International Journal of Multiphase Flow 36 (2010) 798–814

Contents lists available at ScienceDirect

International Journal of Multiphase Flow

journal homepage: www.elsevier.com/locate/ijmulflow

Convective transport of air bubbles in strong hydraulic jumps

Hubert Chanson *

Civil Engineering, The University of Queensland, Brisbane, QLD 4072, Australia

ARTICLE INFO

Article history:
Received 8 January 2010
Received in revised form 26 May 2010
Accepted 28 May 2010
Available online 2 June 2010

Keywords:
Hydraulic jumps
Air bubble entrainment
Turbulent mixing
Convective transport
Strong jumps

ABSTRACT

A hydraulic jump is a flow singularity characterised by a significant amount of air entrainment in the shear zone. The air is entrapped at the jump toe that is a discontinuity between the impinging flow and the roller. The impingement point is a source of air bubbles, as well as a source of vorticity. Herein the convective transport of air bubbles in the jump roller is re-visited. Some analytical extension is presented and the theoretical results are compared with some laboratory experiments conducted in a large-size facility operating at large Froude numbers. The turbulent air bubble mixing coefficient was found to increase linearly with increasing distance and be independent of the Froude and Reynolds numbers. Overall the study highlighted some seminal features of the air–water shear layer in hydraulic jumps with large Froude numbers ($5.1 < Fr_1 < 11.2$). The air bubble entrainment in the mixing zone was a convective transport process, although there was some rapid flow de-aeration for all Froude numbers.

1. Introduction

A hydraulic jump is characterised by a significant amount of air entrainment (Rajaratnam, 1962, 1967; Wisner, 1965). The air is entrapped at the jump toe that is a discontinuity between the impinging flow and the roller (Fig. 1). Fig. 1 illustrates a prototype situation during a flash food. In a hydraulic jump roller, two distinct air–water regions may be distinguished: the air–water shear region and the upper free-surface layer. The air–water shear layer is characterised by a transfer of momentum from the high-velocity jet flow to the recirculation region above, as well as by a convective transport of the entrained air bubbles. In the upper free-surface region, the air–water flow is characterised by an uncontrolled exchange of air and water between the recirculation region and the atmosphere.

The hydraulic jump is classified in terms of its inflow Froude number $Fr_1 = V_1/\sqrt{g \times d_1}$ that is always greater than unity, where V_1 is the inflow velocity, g is the gravity acceleration and d_1 is the upstream flow depth. The physical observations demonstrated that, at large Froude numbers, a hydraulic jump is characterised by a marked roller with a large rate of energy dissipation, some spray and splashing, and some air entrainment (Fig. 1). Some recent reviews include Hager (1992) and Chanson (2009). The first successful air–water flow measurements in hydraulic jumps were conducted by Rajaratnam (1962). Table 1 summarises a number of important contributions, including the milestone study of Resch and Leutheusser (1972) who demonstrated that the bubble entrainment process and energy dissipation are strongly affected by the inflow conditions. To date, most experimental studies were conducted with partially-developed inflow conditions, for which Chanson (1995) highlighted some similarity with the air entrainment process in plunging jets. With partially-developed inflow conditions, the upstream flow is characterised by a developing turbulent boundary layer beneath an ideal fluid flow region. Recently Murzyn and Chanson (2008) re-analysed some Froude similar experiments ($Fr_1 = 5.1$ and 8.5) conducted with Reynolds numbers between 2.4×10^4 and 9.8×10^4. Their results showed some drastic scale effects in the smaller hydraulic jumps in terms of void fraction, bubble count rate and bubble chord time distributions for $Re < 4 \times 10^4$, with lesser entrained air and comparatively larger entrained bubbles in the smallest jumps.

In hydraulic structures, the entrainment of air within hydraulic jumps is studied because of the flow bulking induced by the entrained air and the requirements for higher stilling basin sidewalls downstream of spillways (Hager, 1992; Chanson, 1997). The relevant two-phase flow parameter is the distributions of void fractions. Air entrainment contributes further to some air–water mass transfer (e.g. re-oxygenation) (Avery and Novak, 1978), and the relevant air–water flow properties are the distributions of bubble count rate and of bubble sizes. The entrained bubbles interact also with the turbulence structures, yielding to some turbulent dissipation and the formation of bubble clusters (Chanson, 2007). The study of bubble clustering is relevant to infer whether the formation frequency responds to some particular frequencies of the flow. In hydraulic jumps, the clustering index may provide a measure of the vorticity production rate, of the level of bubble-turbulence

* Tel.: +61 7 33 65 35 16; fax: +61 7 33 65 45 99.
E-mail address: h.chanson@uq.edu.au
URL: http://www.uq.edu.au/~e2hchans/

0301-9322/$ - see front matter © 2010 Elsevier Ltd. All rights reserved.
doi:10.1016/j.ijmultiphaseflow.2010.05.006

(A) General view

(B) Details of the jump roller at high-shutter speed (1/80 s)

Fig. 1. Air entrainment in a hydraulic jump located in a culvert inlet in Brisbane during a flash flood in May 2009 – flow from left to right, Re $\sim 3 \times 10^6$.

interactions and of the associated energy dissipation. Altogether both macro- and micro-scopic air–water flow properties are required to characterise completely the hydraulic jump flow.

In the present study, the convective transport of air bubbles in the hydraulic jump roller is re-visited. Some analytical extension is presented and the theoretical results are compared with some laboratory experiments conducted in a large-size facility operating at large Froude and Reynolds numbers ($3.6 < Fr_1 < 12.4$, $2.9 \times 10^4 < Re < 9.3 \times 10^4$). These conditions are representative of some small full-scale storm waterways and could be considered as a 10:1 scale study of the culvert operation seen in Fig. 1. Herein the focus of the work is on the turbulent mixing and convective transport of air bubbles in the developing shear layer supported by detailed air–water flow properties in hydraulic jumps with large upstream Froude numbers.

2. Convective transport of air bubbles in the mixing layer

In hydraulic jumps with partially-developed inflow conditions, the experimental data demonstrated conclusively that the void fraction distributions exhibited a characteristic shape in the developing shear layer with a local maximum in void fraction (Resch and Leutheusser, 1972; Thandaveswara, 1974; Chanson, 1995). This shape is sketched in Fig. 2 (top right). The void fraction distributions followed closely an analytical solution of the diffusion equation first solved for a hydraulic jump by Chanson (1995, 1997), and the findings are extended herein. The air bubble entrainment is localised at the intersection of the impinging water jet with the receiving body of water. The air bubbles are entrained locally at the toe of the jump (Fig. 2, top left). The impingement perimeter is a source of air bubbles, as well as a source of vorticity. For a small control volume and neglecting the buoyancy and compressibility effects, the continuity equation for air bubbles becomes:

$$V_1 \times \frac{\partial C}{\partial x} + u_r \times \frac{\partial C}{\partial y} = D_t \times \frac{\partial^2 C}{\partial y^2} \quad (1)$$

where C is the void fraction, V_1 is the convection velocity, x is the longitudinal co-ordinate, y is the vertical elevation above the channel bed, the bubble rise velocity u_r is assumed constant, and D_t is the air bubble diffusivity. Eq. (1) is based upon the assumptions of an uniform velocity distribution and constant diffusivity independent of the longitudinal and transverse location. With a change of variable ($X = x - x_1 + u_r/V_1 \times y$), Eq. (1) becomes a two-dimensional diffusion equation (Crank, 1956):

$$V_1 \times \frac{\partial C}{\partial X} = D_t \times \frac{\partial^2 C}{\partial y^2} \quad (2)$$

In the hydraulic jump roller, the air bubbles and packets are entrained at the jump toe acting as a point source located at ($x - x_1 = 0$, $y = d_1$), where d_1 is the upstream flow depth (Fig. 2). The strength of the source equals Q_{air}/W, where Q_{air} is the entrained air volume and W is the channel width. Eq. (2) may be solved by applying the method of images assuming a diffusivity independent of the vertical co-ordinate y and an advection velocity independent of x. The complete analytical solution is:

$$C = \frac{\frac{Q_{air}}{Q}}{\sqrt{4 \times \pi \times D^{\#} \times X'}} \times \left(\exp\left(-\frac{(y'-1)^2}{X'} \right) + \exp\left(-\frac{(y'+1)^2}{X'} \right) \right) \quad (3)$$

where $X' = X/d_1$, $y' = y/d_1$, and $D^{\#}$ is a dimensionless diffusivity: $D^{\#} = D_t/(V_1 \times d_1)$. In the right-hand side term of Eq. (3), the first term is the contribution of the real source (i.e. jump toe) and the second term is the contribution of the imaginary source located at ($x - x_1 = 0$, $y = -d_1$).

Remark. A simpler solution was proposed earlier in the form of (Chanson, 1995):

$$C = C_{max} \times \exp\left(-\frac{1}{4 \times D^{\#}} \times \frac{\left(\frac{y - Y_{Cmax}}{d_1}\right)^2}{\left(\frac{x - x_1}{d_1}\right)} \right) \quad (4)$$

where Y_{Cmax} is the location where the void fraction is maximum in the developing shear layer. Eq. (4) is a limiting case of Eq. (3) assuming that the effects of buoyancy are accounted for by Y_{Cmax}, the contribution of the imaginary source term is small, and $C_{max} = (Q_{air}/Q)/\sqrt{4 \times \pi \times D^{\#} \times X'}$.

Note that Eq. (3) is restricted to the air–water shear layer corresponding typically to $y < y^*$, where y^* is the local minimum in void fraction between the bubbly shear flow region and the upper free-surface region (Fig. 2, top right).

3. Experimental setup

The experiments were performed in the Gordon McKay Hydraulics Laboratory at the University of Queensland. The channel was horizontal, 3.2 m long and 0.5 m wide. The sidewalls were

Table 1
Experimental investigations of air–water flow properties in hydraulic jumps.

Reference (1)	d_1 (2)	Fr_1 (3)	Re (4)	x_1 (m) (5)	W (m) (6)	Instrumentation (7)
Laboratory studies						
Rajaratnam (1962)	0.0254	2.7–8.7	3.4×10^4–1.1×10^5	–	0.31	Conductivity probe
Resch and Leutheusser (1972)	0.039 and 0.012	3.0–8.0	9.7–2.4×10^4	0.39–7.8	0.39	Hot-film probe (∅ = 0.6 mm)
Babb and Aus (1981)	0.035	6.0	1.2×10^5	–	0.46	Hot-film probe (∅ = 0.4 mm)
Chanson (1995)	0.016–0.017	5.0–8.1	3.1–5.0×10^4	0.7–0.96	0.25	Single-tip phase-detection probe (∅ = 0.35 mm)
Mossa and Tolve (1998)	0.0185–0.020	6.42–7.3	5.2–6.2×10^4	0.90	0.40	Video-imaging
Chanson and Brattberg (2000)	0.014	6.3 and 8.5	3.3 and 4.4×10^4	0.50	0.25	Dual-tip phase-detection probe (∅ = 0.025 mm)
Murzyn et al. (2005)	0.021–0.059	2.0–4.8	8.8–4.6×10^4	0.35	0.30	Dual-tip phase-detection probe (∅ = 0.010 mm)
Chanson (2007)	0.013–0.029	5.1–8.6	2.5–9.8×10^4	0.50 and 1.0	0.25 and 0.50	Single-tip phase-detection probe (∅ = 0.35 mm)
Gualtieri and Chanson (2007)	0.012	5.2–14.3	2.4–5.8×10^4	0.50	0.25	Single-tip phase-detection probe (∅ = 0.35 mm)
Kucukali and Chanson (2008)	0.024	4.7–6.9	5.4–8.0×10^4	1.0	0.50	Single-tip and dual-tip phase-detection probes (∅ = 0.35 and 0.25 mm)
Murzyn and Chanson (2009)	0.018	5.1–8.3	3.8–6.2×10^4	0.75	0.50	Dual-tip phase-detection probe (∅ = 0.25 mm)
Field study						
Valle and Pasternack (2006)	0.22*	2.8*	9×10^5	–	2	Time domain reflectometry (TDR)
Present study	0.018–0.019	3.6–12.4	2.9–9.3×10^4	0.75	0.50	Visual and video observations
	0.0185	5.14	4.0×10^4	0.75	0.50	Dual-tip phase-detection probe (∅ = 0.25 mm) measurements
	0.018	7.47	5.6×10^4			
	0.018	9.21	6.9×10^4			
	0.018	10.0	7.5×10^4			
	0.01783	11.2	8.3×10^4			

Notes: d_1: upstream flow depth; Fr_1: upstream Froude number ($Fr_1 = V_1/\sqrt{g \times d_1}$); Re: Reynolds number (Re = $\rho \times V_1 \times d_1/\mu$); W: channel width; x_1: distance between the upstream gate and jump toe.
* Corrected data.

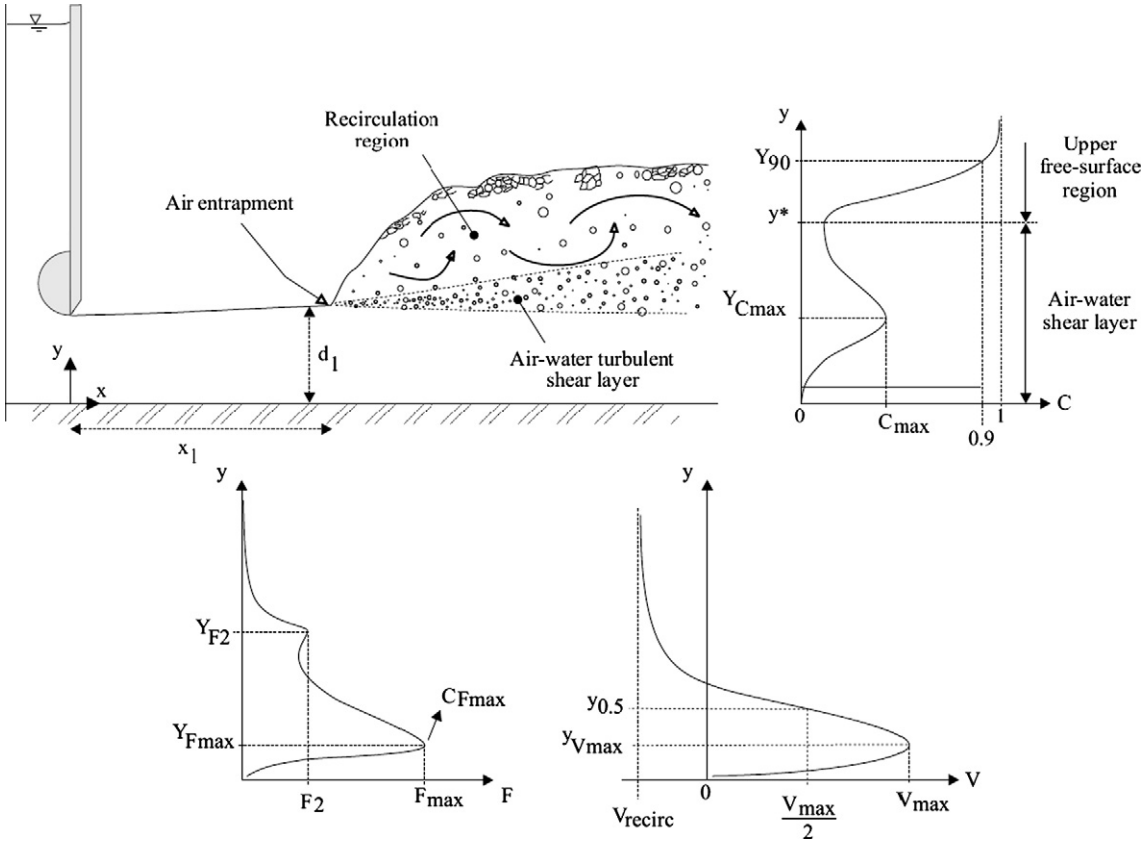

Fig. 2. Sketch of air bubble entrainment in hydraulic jumps with partially-developed inflow conditions – top left. Air water flow regions – top right. Vertical distribution of void fraction in the hydraulic jump roller – bottom left. Vertical distribution of bubble count rate – bottom right. Vertical distribution of velocity.

made of 3.2 m long, 0.45 m high glass panels and the bed was made of 12 mm thick PVC sheets. The inflow was controlled by an upstream undershoot gate, and the downstream flow conditions were controlled by a vertical overshoot gate. The same flume was used previously by Chanson (2007), Kucukali and Chanson (2008) and Murzyn and Chanson (2009), but new flow conditions were tested herein (Table 1).

The channel was fed by a constant head tank. The water discharge was measured with a Venturi meter located in the supply line that was calibrated on-site with a large V-notch weir. The discharge measurements were accurate within ±2%. The clear-water flow depths were measured using rail mounted point gauges with a 0.2 mm accuracy. The inflow conditions were controlled by a vertical gate with a semi-circular rounded shape ($\varnothing$ = 0.3 m) and the downstream coefficient of contraction was about unity. The upstream gate aperture was fixed during all experiments (h = 0.018 m).

Additional information was obtained with some digital cameras, while some movies of the experiments were presented by Chanson (2009b) together with the complete data sets.

3.1. Air–water flow instrumentation

The air–water flow properties were measured with a double-tip phase-detection probe. The probe was equipped with two identical sensors with an inner diameter of 0.25 mm. The longitudinal distance between probe tips was Δx = 6.96 mm while the transverse separation distance between tips was Δz = 2.08 mm. The displacement and the position of the probe in the vertical direction were controlled by a fine adjustment system connected to a Mitutoyo™ digimatic scale unit with a vertical accuracy of less than 0.1 mm. The dual-tip probe was excited by an electronic system (Ref. UQ82.518) designed with a response time of less than 10 μs. During the experiments, each probe sensor was sampled at 20 kHz for 45 s. The analysis of the probe voltage output was based upon a single-threshold technique, with a threshold set between 45% and 55% of the air–water voltage range. The single-threshold technique is a robust method that is well-suited to free-surface flows (Toombes, 2002; Chanson and Carosi, 2007).

The processing of the probe signal yielded a number of air–water flow properties, including the void fraction C defined as the volume of air per unit volume of air and water, the bubble count rate F defined as the number of bubbles impacting the probe tip per second, and the air chord time distributions where the chord time is defined as the time spent by the bubble on the probe tip.

The air–water interfacial velocity V was calculated as $V = \Delta x/T$, where Δx is the longitudinal distance between both tips (Δx = 6.96 mm) and T is the average air–water interfacial time between the two probe sensors (Crowe et al., 1998; Chanson, 1997, 2002). T was deduced from a cross-correlation analysis. The turbulence level Tu characterised the fluctuations of the air–water interfacial velocity between the probe sensors. It was deduced from the shapes of the cross-correlation R_{xz} and auto-correlation R_{xx} functions (Chanson and Toombes, 2002; Chanson, 2002). The analysis of the probe signal time series provided further information on the bubble chord times and the longitudinal air–water structure of the flow.

3.2. Experimental flow conditions

For all experiments, the jump toe was located at a distance x_1 = 0.75 m from the upstream rounded gate and the same gate opening h = 0.018 m was used for the whole study. For these conditions, the inflow depth ranged from 0.0178 to 0.019 m depending upon the flow rate (Table 1, column 2). Based on previous experiments made with the same experimental facility (Chanson, 2005), the inflow was characterised by a partially-developed boundary layer.

Two series of experiments were conducted (Table 1). The first series focused on the visual properties of hydraulic jumps. The experiments were performed with inflow Froude numbers between 3.4 and 12.4 corresponding to Reynolds numbers between 2.9×10^4 and 9.3×10^4. In the second series of experiments, some detailed air–water flow measurements at the sub-millimetric scale were conducted using the double-tip phase-detection probe. The flow conditions corresponded to Froude numbers between 5.1 and 11.2 and Reynolds numbers between 4×10^4 and 8.3×10^4, although the focus of the study was on the hydraulics jumps with large Froude and Reynolds numbers ($Fr_1 > 7$, $Re > 5 \times 10^4$).

4. Basic air–water flow properties

4.1. Flow patterns

The hydraulic jump marked a singularity in terms of the flow depth, and the velocity and pressure fields. It was characterised by the development of large-scale turbulence in the roller. At the jump toe, the air bubbles and air packets were entrained into a developing shear layer that was characterised by some intensive turbulence production of large coherent vortices with horizontal axes perpendicular to the flow direction (Fig. 2). The air entrainment took place in the form of air bubbles and pockets entrapped at the impingement of the upstream supercritical flow with the jump roller. The air pockets were broken up in smaller air bubbles as they were advected downstream in the shear region that was characterised by some large void fractions and bubble count rates. In the recirculating region above the developing shear layer, some unsteady flow reversal and recirculation took place. The high-speed photographs showed a significant amount of air–water ejections and splashes above the roller (Fig. 3). The ejected packets took different forms ranging from elongated fingers to single droplets and air–water packets, and Fig. 3 presents some photographic examples.

The location of the jump toe was constantly fluctuating around an average position ($x = x_1$). The jump toe pulsations were caused by the growth, advection and pairing of large-scale vortices in the developing shear layer (Long et al., 1991; Habib et al., 1994). Herein the toe oscillation frequencies F_{toe} were typically about 0.3–0.8 Hz (Table 2, column 7). The results are summarised in Fig. 4 where they are compared with earlier studies. The frequency F_{ej} of the large-scale vortical structures as well as their advection velocity V_{ej} were also recorded using some frame-by-frame replay of video-records at 30 fps, and tracking the large coherent structures in the developing shear layer (Table 2, columns 8 and 9). The data are presented in Figs. 4 and 5. Herein F_{ej} represents the rate of production of large-scale coherent structures advected in the developing shear layer. Fig. 4 summarises the observations in terms of the Strouhal numbers $F_{toe} \times d_1/V_1$ and $F_{ej} \times d_1/V_1$ as functions of the Reynolds number $\rho \times V_1 \times d_1/\mu$. The data are compared with the jump toe fluctuation data of Long et al. (1991), Mossa and Tolve (1998), Chanson (2007) and Murzyn and Chanson (2009). Noteworthy the jump toe fluctuation frequencies F_{toe} were almost equal to the production rate F_{ej} of large-scale vortical structures. The finding supported the assertion that the jump toe oscillations are caused by the formation and downstream advection of large-scale vortices in the shear layer.

Fig. 5 presents the dimensionless advection speed V_{ej}/V_1 of the large-scale coherent structures in the developing shear layer. The advection speed represented the average convection velocity of the large coherent structures in the mixing layer. The data were

(A) Looking downstream at the jump toe with the probe tip located at $x\text{-}x_1 = 0.075$ m - $Fr_1 = 5.1$, $Re = 4.0\times10^4$, $d_1 = 0.0185$ m, $x_1 = 0.75$ m, shutter speed: 1/80 s

(B) Looking upstream at the splashes above roller with the probe tip located at $x\text{-}x_1 = 0.150$ m - $Fr_1 = 7.5$, $Re = 5.6\times10^4$, $d_1 = 0.018$ m, $x_1 = 0.75$ m, shutter speed: 1/80 s

(C) $Fr_1 = 7.5$, $Re = 5.6\times10^4$, $d_1 = 0.018$ m, $x_1 = 0.75$ m, shutter speed: 1/80 s - From Top Left, anti-clockwise: (C1) Side view with the probe tip located at $x\text{-}x_1 = 0.075$ m; (C2) Looking upstream above the roller with the probe tip located at $x\text{-}x_1 = 0.075$ m; (C3) Looking upstream above the roller with the probe tip located at $x\text{-}x_1 = 0.35$ m; (C4) Looking downstream at the jump toe with the probe tip located at $x\text{-}x_1 = 0.35$ m

Fig. 3. High-shutter speed photographs of air–water projections above the hydraulic jump roller.

Table 2
Measured flow properties of hydraulic jumps (present study).

Q (m^3/s) (1)	V_1 (m/s) (2)	Fr_1 (3)	Re (4)	d_1 (m) (5)	d_2 (m) (6)	F_{toe} (Hz) (7)	F_{ej} (Hz) (8)	V_{ej} (m/s) (9)
0.0147	1.55	3.6	2.9×10^4	0.019	0.089	0.492	0.533	0.67
0.0166	1.75	4.0	3.3×10^4	0.019	0.104	0.392	0.2	0.75
0.02225	2.34	5.4	4.4×10^4	0.019	0.138	0.509	0.42	0.61
0.0282	3.13	7.5	5.6×10^4	0.018	0.178	0.833	0.733	0.75
0.03255	3.52	8.3	6.5×10^4	0.0185	0.206	–	0.533	1.06
0.0367	4.08	9.7	7.3×10^4	0.018	0.23	–	0.793	1.27
0.0378	4.20	10.0	7.5×10^4	0.018	–	0.714	–	–
0.0399	4.43	10.6	7.9×10^4	0.018	0.246	–	1.099	1.20
0.04175	4.68	11.2	8.3×10^4	0.0178	–	0.765		–
0.047	5.22	12.4	9.3×10^4	0.018	0.258	–	1	1.69

Notes: d_1: upstream flow depth; d_2: downstream flow depth; Fr_1: upstream Froude number; F_{ej}: large-scale vortical structure ejection frequency; F_{toe}: jump toe horizontal oscillation frequency; Q: water discharge; Re: Reynolds number; V_{ej}: advection velocity of large-scale vortical structures; V_1: upstream flow velocity; (–): data not available.

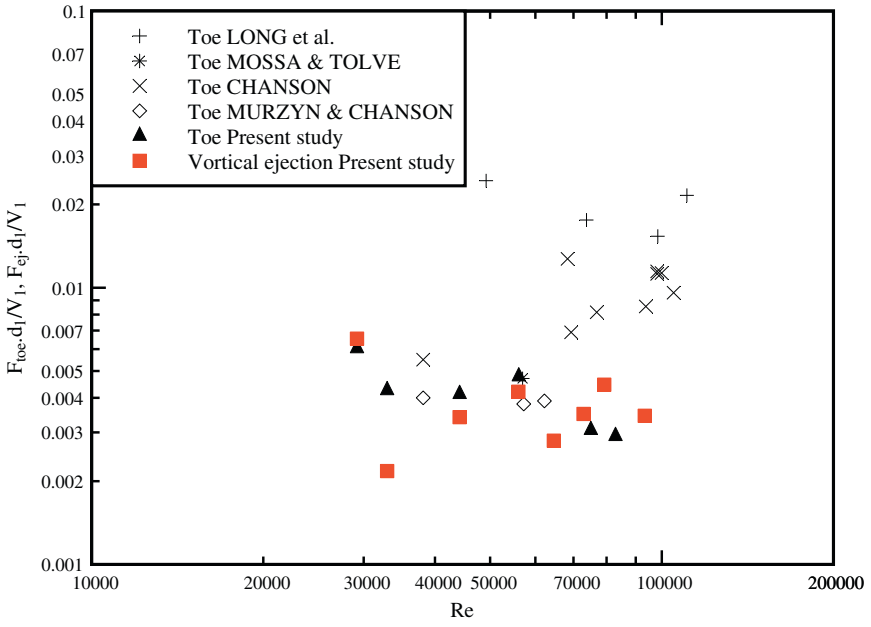

Fig. 4. Dimensionless relationship between Strouhal number and Reynolds number in hydraulic jumps: oscillations of the jump toe (Data: Long et al., 1991; Mossa and Tolve, 1998; Chanson, 2007; Murzyn and Chanson, 2009, present study) and ejection frequency of large-scale vortical structures (Data: present study).

nearly independent of the Reynolds number and they yielded in average: $V_{ej}/V_1 = 0.32$ for $5.1 < Fr_1 < 11.2$. For comparison, the observations of Brown and Roshko (1974) gave a convective speed $V_{ej}/\Delta V \approx 0.24$ in a free shear layer with a transverse velocity gradient ΔV.

4.2. Void fraction and bubble count rate distributions

In the air–water shear layer, the void fraction profiles followed closely an analytical solution of the convective transport of air bubbles (Eq. (3)). This is seen in Fig. 6 at four longitudinal locations in a hydraulic jump ($Fr_1 = 11.2$). In practice, the comparison between experimental data and theoretical results showed that, in Eq. (3), the effects of the imaginary source term were small, and the effects of buoyancy were best accounted for using the measured location of the maximum void fraction (Y_{Cmax}) (Eq. (4)).

Some typical values of the dimensionless turbulent air bubble mixing coefficients $D^{\#} = D_t/(V_1 \times d_1)$ are presented in Fig. 7A as a function of the Reynolds number Re. Herein the turbulent mixing coefficient was deduced from the best data fit. Despite some scatter, the diffusivity data yielded an average dimensionless diffusivity $D_t/(V_1 \times d_1) = 0.044$ for all three experimental data sets (Chanson, 1997, 2007; Chanson and Brattberg, 2000) and an average value of 0.042 for the present set of experiments. Within the range of experiments, the dimensionless diffusivity was found to be independent of the inflow Froude number and Reynolds numbers, although the data suggested some increase in $D^{\#}$ with increasing distance $(x - x_1)/d_1$ from the jump toe. This is illustrated in Fig. 7B. For the present study, the data were best correlated by:

$$D^{\#} = 0.01 + 0.0012 \times \frac{x - x_1}{d_1}, \quad \text{for } 5 < \frac{x - x_1}{d_1} < 70 \tag{5}$$

for $7 < Fr_1 < 11.5$ with a normalised correlation coefficient of 0.925. Eq. (5) is compared with the experimental data in Fig. 7B. It is noteworthy to consider the longitudinal variation of the momentum exchange coefficient (or "eddy viscosity") in a developing shear layer. Goertler's (1942) solution of the Navier–Stokes equations implies a longitudinal distribution of the "eddy viscosity" function:

$$\frac{\nu_T}{V_1 \times d_1} = \frac{1}{4 \times K} \times \frac{x - x_1}{d_1} \tag{6}$$

where K is a constant equal to 9–13.5 in monophase flows (Rajaratnam, 1976; Schlichting, 1979), and 4–10 in air–water flows

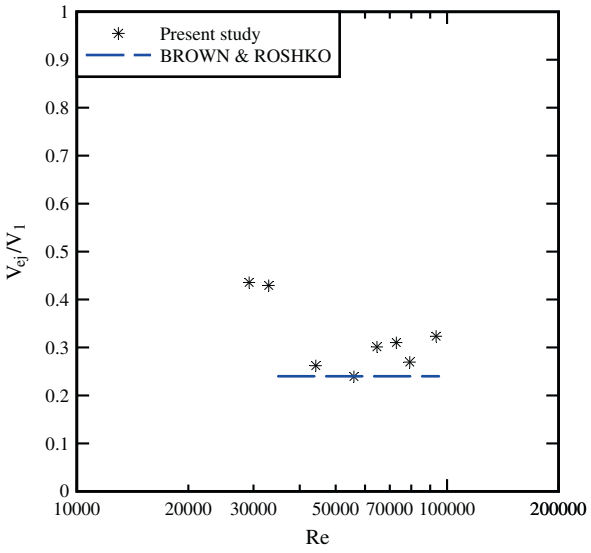

Fig. 5. Dimensionless advection speed of the large-scale vortical structures in the developing shear layer of hydraulic jumps: comparison between the present data and the observations of Brown and Roshko (1974) in a free shear layer.

(Chanson, 1997). Eqs. (5) and (6) show a same linear trend but with different coefficients.

In the air–water shear layer, the void fraction distributions showed a local maximum in void fraction C_{max}. That local maximum C_{max} decreased with increasing distance $(x - x_1)$ from the impingement point while the diffusion layer broadened as illustrated in Fig. 6. The data are summarised in Fig. 8A, where the maximum void fraction C_{max} is plotted a function of the dimensionless longitudinal distance $(x - x_1)/d_1$ from the jump toe. The present data are compared with earlier data sets and all the data followed some exponential decay:

$$C_{max} \propto \exp\left(-\frac{x - x_1}{d_1}\right) \quad (7)$$

Some typical vertical profiles of bubble count rate are presented also in Fig. 6. Each profile exhibited a maximum count rate F_{max} in the air–water shear layer and a secondary peak F_2 in the upper free-surface region. Both definitions are sketched in Fig. 2 (bottom left). The maximum bubble count rate F_{max} was linked with a region of maximum shear stress. Noteworthy its location Y_{Fmax} was consistently below the location Y_{Cmax} of maximum void fraction in the air–water shear layer, possibly because of some buoyancy effect.

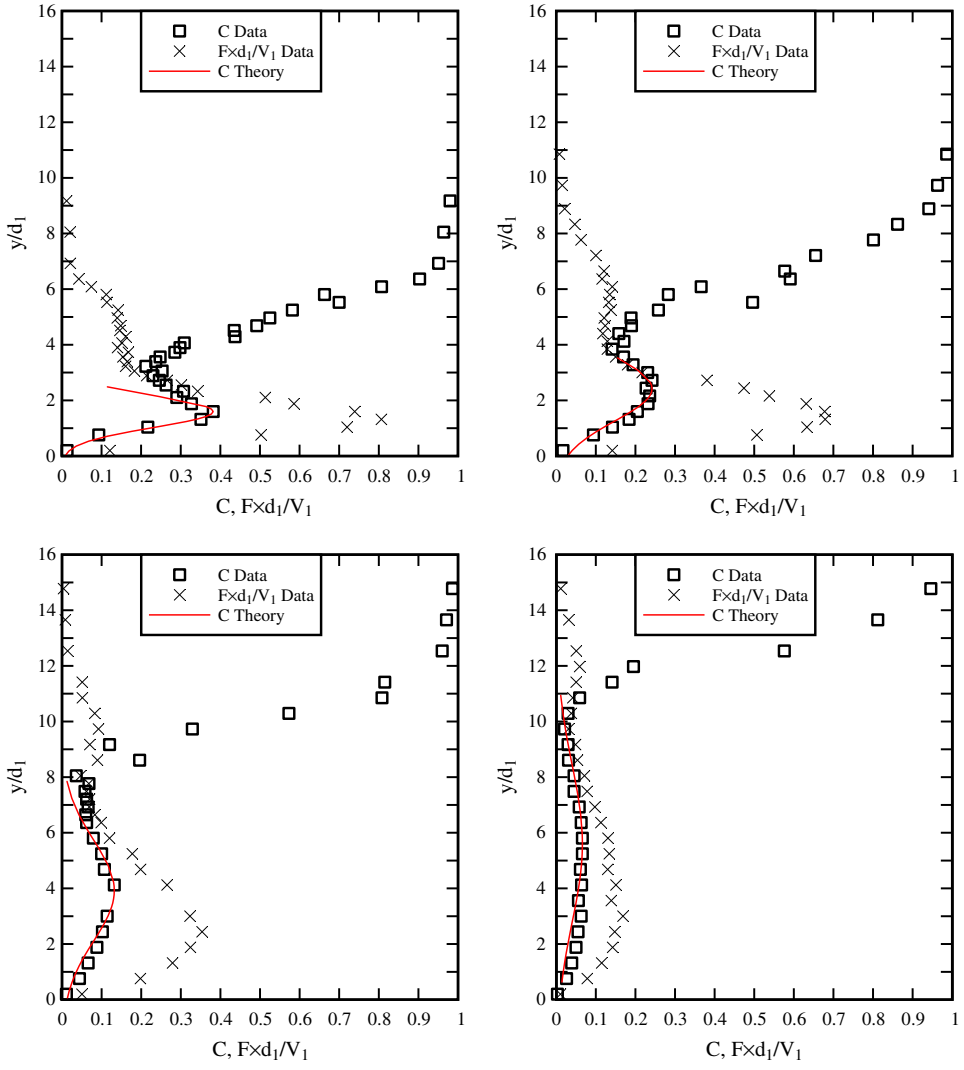

Fig. 6. Dimensionless distributions of void fraction in the air–water shear layer: comparison between experimental data and theoretical model ($Fr_1 = 11.2$, $Re = 8.3 \times 10^4$, $d_1 = 0.01783$ m, $x_1 = 0.75$ m) – from left to right. Top to bottom: $(x - x_1)/d_1 = 12.6$, 19.6, 36.4 and 50.5.

The diffusion layer did not coincide with the momentum shear layer highlighting a double diffusion process whereby air bubbles and vorticity diffused in the shear region at different rates and in a different manner. The non-coincidence of C_{max} and F_{max} demonstrated that the interactions between the developing shear layer and air diffusion layer were complex.

Fig. 8B presents the longitudinal distribution of the maximum bubble count rate in the hydraulic jump. The present data series were compared with earlier studies and the results showed an exponential decay in maximum bubble count rate:

$$\frac{F_{max} \times d_1}{V_1} \propto \exp\left(-\frac{x - x_1}{d_1}\right) \quad (8)$$

It is worthwhile to highlight that, for the present data set, the longitudinal distributions of maximum bubble count rate in the shear region seemed to reach an asymptotic profile at the largest Froude numbers ($Fr_1 > 9$):

$$\left(\frac{F_{max} \times d_1}{V_1}\right)_{asymptot} = 1.08 - 0.018 \times \frac{x - x_1}{d_1}, \quad \text{for } Fr_1 > 9 \text{ and } (x - x_1)/d_1 < 60 \quad (9)$$

Eq. (9) is shown in Fig. 8B: it illustrates an upper limit of maximum bubble count rate in the air–water shear region. It is unknown whether the asymptotic trend (Eq. (9)) is linked with a physical process or a limitation of the metrology.

Several characteristic air–water flow parameters are regrouped in Fig. 9, including the dimensionless location Y_{Cmax}/d_1 where the void fraction is maximum, Y_{Fmax}/d_1 corresponding to the location where the bubble count rate is maximum, the location y^*/d_1 corresponding to the boundary between the air–water shear layer and

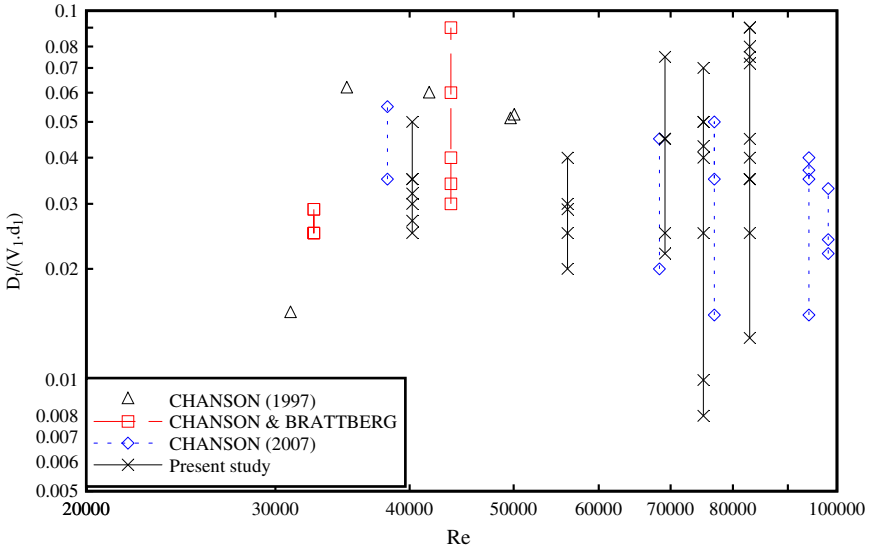

(A) $D_t/(V_1 \times d_1)$ as a function of the Reynolds number $Re = \rho \times V_1 \times d_1/\mu$

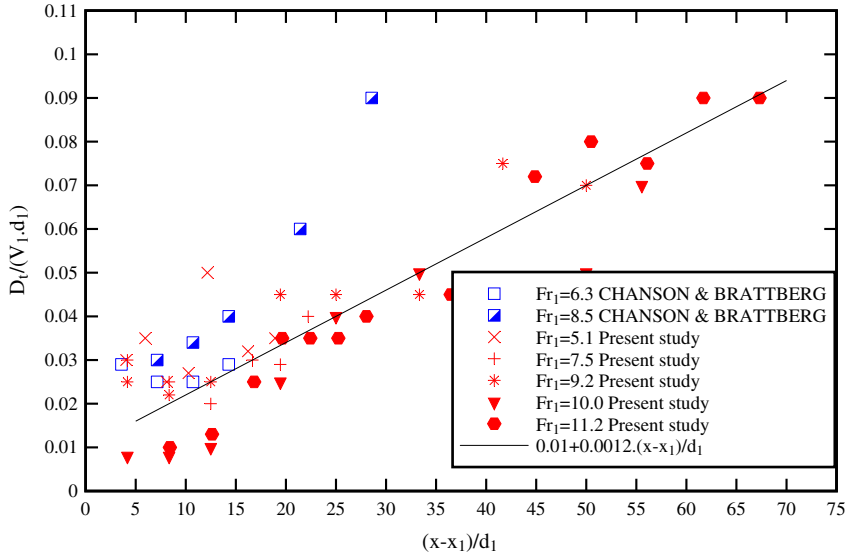

(B) $D_t/(V_1 \times d_1)$ as a function of dimensionless distance from the jump toe $(x\text{-}x_1)/d_1$ - Comparison with Equation (5)

Fig. 7. Dimensionless turbulent diffusivity of air bubbles in the developing shear layer of hydraulic jumps: Experimental data: Chanson (1997, 2007), Chanson and Brattberg (2000) and present study.

the upper free-surface region and Y_{90}/d_1 corresponding to the location where $C = 0.90$. The notation is explained in Fig. 2. The data showed systematically that:

$$\frac{Y_{Fmax}}{d_1} < \frac{Y_{Cmax}}{d_1} < \frac{y_*}{d_1} < \frac{Y_{90}}{d_1} \quad (10)$$

4.3. Velocity and turbulent intensity distributions

The air–water velocity measurements were conducted with the dual-tip conductivity probe based upon the mean travel time between the probe sensors and the distance between probe sensors ($\Delta x = 6.96$ mm). Some typical results are presented in Fig. 10 for two Froude numbers ($Fr_1 = 9.2$ and 10.0). The graphs present the dimensionless interfacial velocities V/V_{max} in the hydraulic jump roller, where V_{max} is the maximum velocity in a cross-section, measured at $y = Y_{Vmax}$. At the channel bed, a no-slip condition imposed $V(y = 0) = 0$. All the velocity profiles exhibited a similar shape despite some scatter. In the developing shear layer, the velocity profiles followed some wall jet pattern (Rajaratnam, 1965; Chanson and Brattberg, 2000). The dimensionless distributions of interfacial velocities were best fitted by:

$$\frac{V}{V_{max}} = \left(\frac{y}{Y_{Vmax}}\right)^{\frac{1}{N}}, \quad \text{for } \frac{y}{Y_{Vmax}} < 1 \quad (11)$$

$$\frac{V - V_{recirc}}{V_{max} - V_{recirc}} = \exp\left(-\frac{1}{2}\left[1.765\left(\frac{y - Y_{Vmax}}{y_{0.5}}\right)\right]^2\right), \quad \text{for } 1 < \frac{y}{Y_{Vmax}} < 3 \text{ to } 4 \quad (12)$$

where V_{recirc} is the recirculation velocity measured in the upper free-surface region, $y_{0.5}$ is the vertical elevation where $V = V_{max}/2$

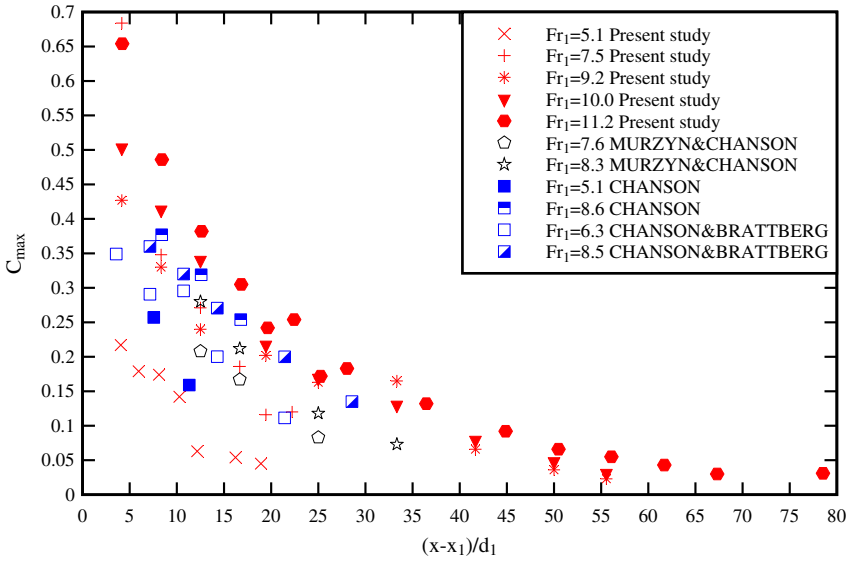

(A) Maximum void fraction in the air-water shear layer

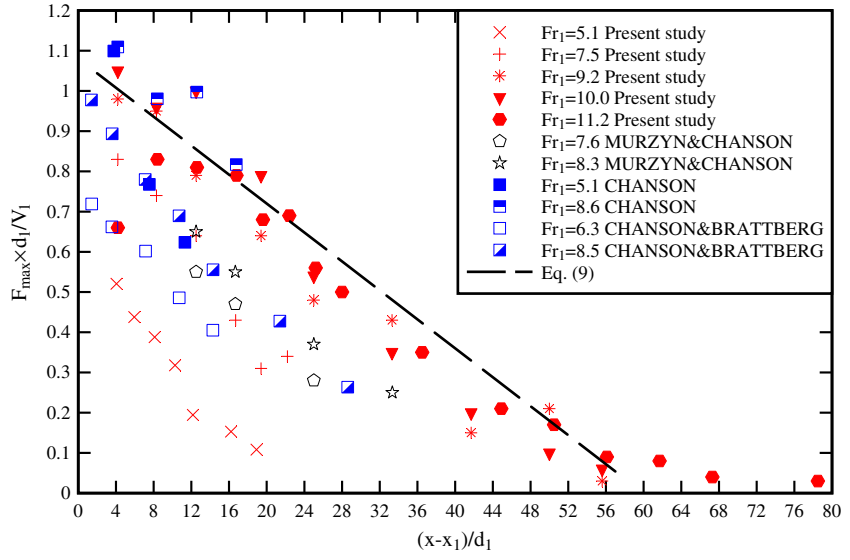

(B) Maximum bubble count rate in the air-water shear layer - Comparison with Equation (9)

Fig. 8. Dimensionless longitudinal distributions of maximum void fraction C_{max} and bubble count rate $F_{max} \times d_1/V_1$ in the air–water shear layer: comparison between the present data set and the data of Chanson and Brattberg (2000), Chanson (2007) and Murzyn and Chanson (2009).

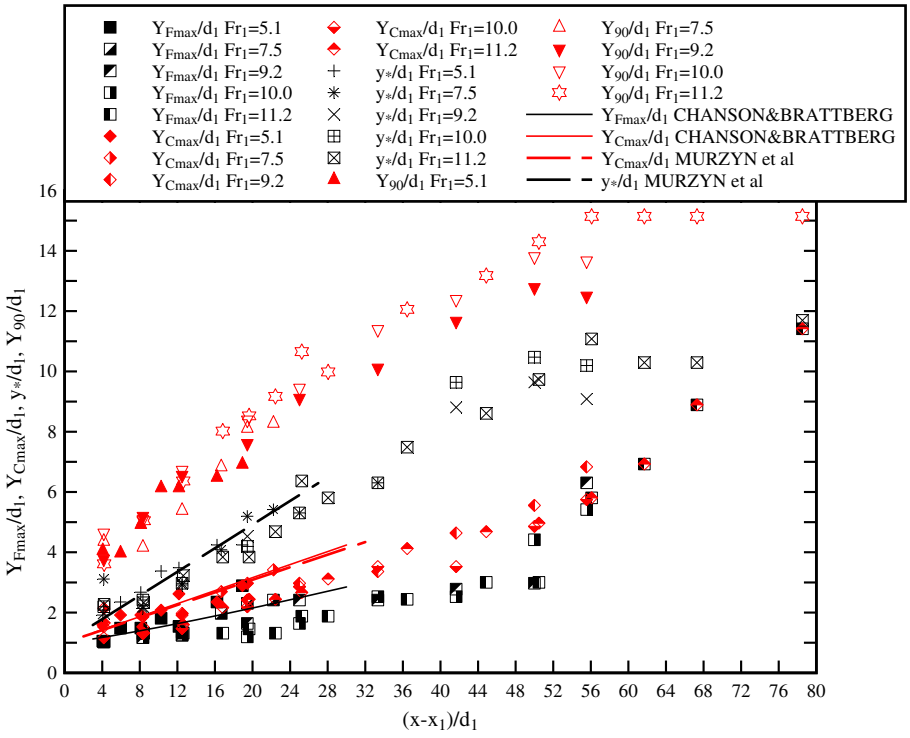

Fig. 9. Longitudinal distributions of the dimensionless distances Y_{Fmax}/d_1, Y_{Cmax}/d_1, y^*/d_1 and Y_{90}/d_1: comparison between the present experimental data and the data of Chanson and Brattberg (2000) and Murzyn et al. (2005).

and N is a constant ($N \approx 6$). The present results followed closely the above equations, despite some data scatter caused by the unsteady and fluctuating nature of the flow (Fig. 10). This is illustrated in Fig. 10 where the data are shown in a self-similar presentation and compared with Eq. (12).

The maximum velocity data V_{max} showed a longitudinal decay with increasing distance from the jump toe (Fig. 11). They compared favourably with earlier observations as shown in Fig. 11. All the data followed closely the empirical correlation:

$$\frac{V_{max}}{V_1} = \exp\left(-0.028 \times \frac{x-x_1}{d_1}\right), \quad \text{for } 0 < \frac{x-x_1}{d_1} < 80 \tag{13}$$

Eq. (13) is compared with the experimental data in Fig. 11.

In the recirculation region above the mixing zone, the present data indicated some negative time-averaged velocity (Fig. 10). This is sketched in Fig. 2 (bottom right). For the present experiments, the recirculation velocity satisfied in average: $V_{recirc}/V_{max} = -0.4$. While the probe design was not well suited for some negative

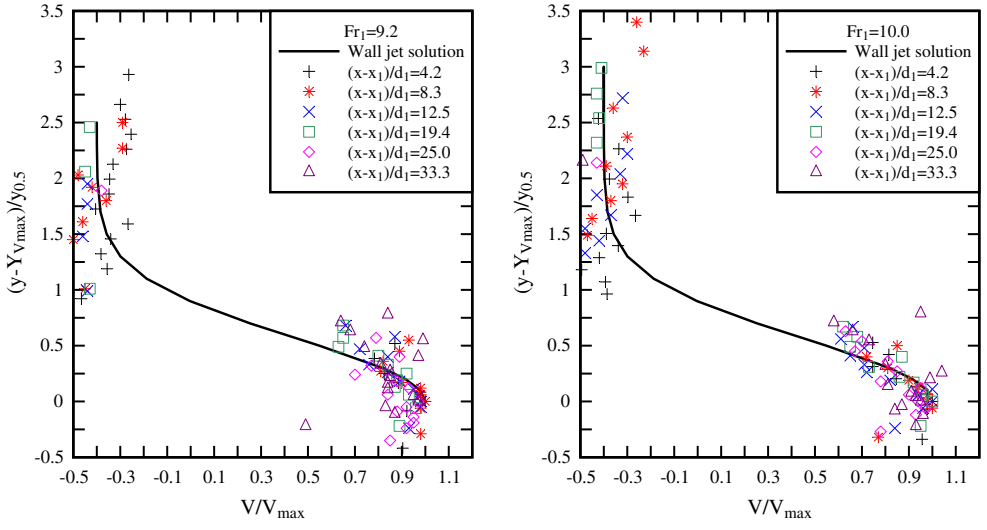

(A, Left) $Fr_1 = 9.2$, $Re = 6.9\times10^4$, $d_1 = 0.018$ m, $x_1 = 0.75$ m

(B, Right) $Fr_1 = 10.0$, $Re = 7.5\times10^4$, $d_1 = 0.018$ m, $x_1 = 0.75$ m

Fig. 10. Dimensionless velocity distributions in hydraulic jumps: comparison between experimental data and Eq. (12).

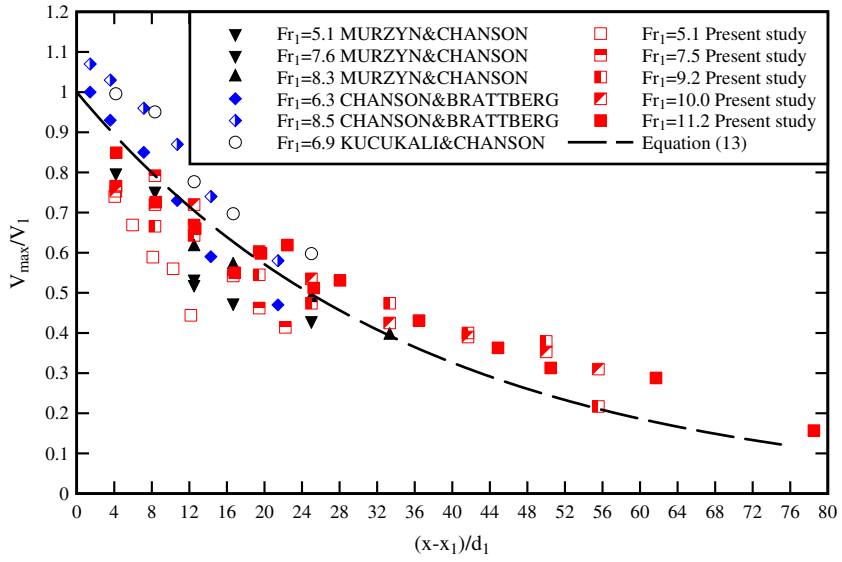

Fig. 11. Longitudinal distribution of dimensionless maximum velocity V_{max}/V_1 in hydraulic jumps: comparison between the present data, the data of Chanson and Brattberg (2000), Kucukali and Chanson (2008), and Murzyn and Chanson (2009), and Eq. (13).

velocity measurements because the signals were adversely affected by the probe support wake, the present findings demonstrated that some recirculation velocity data could be qualitatively observed with the dual-tip probe.

The turbulence intensity v_x'/V_1 was derived from a cross-correlation analysis between the two probe sensor signals. This approach was based on the width of the cross-correlation function relative to that of the auto-correlation function (Chanson and Toombes, 2002). The turbulence level v_x'/V_1 characterised the fluctuations of the interfacial air–water velocity. Fig. 12 presents some typical vertical distributions of turbulence intensity. The results showed some very high levels of turbulence, possibly linked with the bubble induced turbulence in the jump shear region, together with some basic assumptions underlying the turbulence intensity estimates (Chanson and Toombes, 2002). In the mixing zone ($y/d_1 < 5$–6), the turbulence levels increased with increasing distance from the bed y/d_1 and with increasing Froude number. The former is seen in both Fig. 12A and B, while the latter trend is illustrated by comparing Fig. 12 A ($Fr_1 = 10$) and B ($Fr_1 = 11.2$).

Overall the present results were consistent with those obtained by Kucukali and Chanson (2008) and Murzyn and Chanson (2009), and they covered a wider range of flow conditions, especially for large Froude numbers (Table 1). In the upper free-surface region and recirculation region ($y/d_1 > 6$), lower turbulence levels were observed. But it must be stressed that the probe design was not well suited for measurements in the recirculation region.

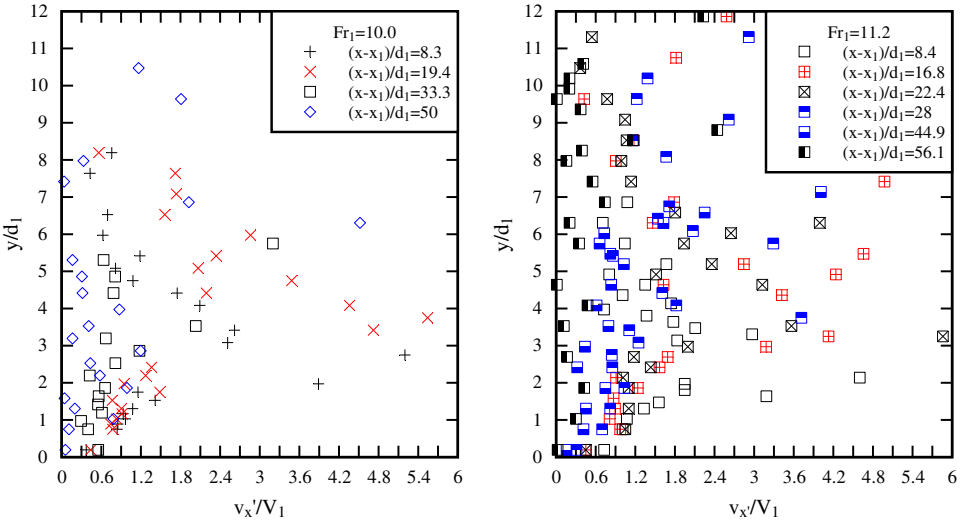

(A, Left) $Fr_1 = 10.0$, $Re = 7.5\times10^4$, $d_1 = 0.018$ m, $x_1 = 0.75$ m

(B, Right) $Fr_1 = 11.2$, $Re = 8.3\times10^4$, $d_1 = 0.0178$ m, $x_1 = 0.75$ m

Fig. 12. Dimensionless distributions of turbulence intensity v_x'/V_1 in hydraulic jumps.

5. Air–water chord properties

The time-averaged air–water properties such as void fraction, interfacial velocity, bubble count rate did not provide any information on the micro-scopic structure of the two-phase flow. Herein the air–water chord properties including the longitudinal structure of air and water were measured and analysed.

5.1. Bubble chord time distributions

The bubble chord times were recorded for all investigated flow conditions. The bubble chord time is proportional to the bubble chord length and inversely proportional to the velocity. In a complicated flow such as a hydraulic jump, some flow reversal and recirculation exist, and the phase-detection intrusive probes cannot discriminate accurately the direction nor magnitude of the velocity. The small bubble chord times corresponded to small bubbles passing rapidly in front the probe sensor, while large chord times implied large air packet flowing slowly past the probe sensor. For intermediate chord times, there were a wide range of possibilities in terms of bubble sizes depending upon the bubble velocity.

Figs. 13 and 14 show some typical normalised bubble chord time distributions for two inflow Froude numbers. Fig. 13 presents some data in the air–water shear layer at the characteristic location Y_{Fmax} where the bubble count rate was maximum ($F = F_{max}$). Fig. 14 illustrates some data in the upper free-surface region at the location of the secondary peak in bubble count rate ($F = F_2$ and $y = Y_{F2}$). For each figure, the legend provides the location ($x - x_1$, y/d_1) and the local air–water flow properties (C, F, V). The histogram columns represent each the probability of droplet chord

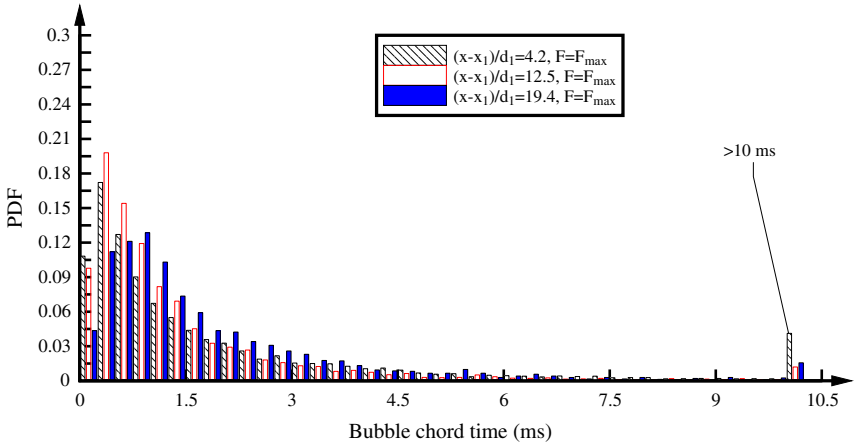

$(x-x_1)/d_1$	y/d_1	C	$F \times d_1/V_1$	V/V_1
4.17	1.03	0.407	0.826	0.752
12.50	1.36	0.185	0.645	0.599
19.44	2.31	0.107	0.310	0.414

(A) $Fr_1 = 7.5$, $Re = 5.6 \times 10^4$, $d_1 = 0.018$ m, $x_1 = 0.75$ m

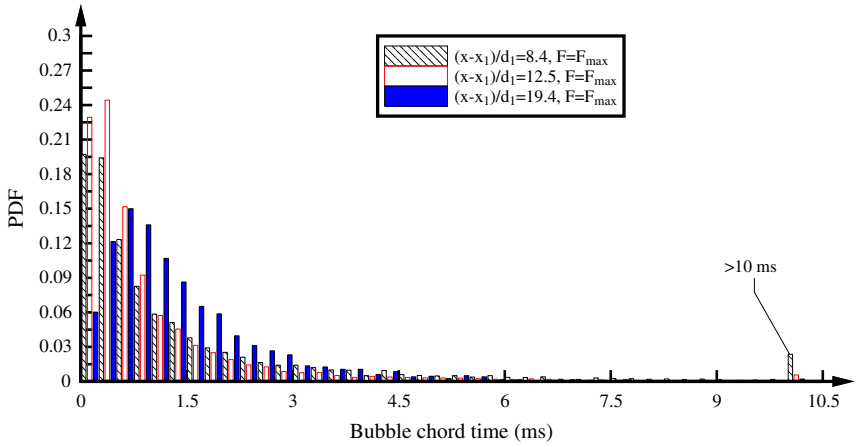

$(x-x_1)/d_1$	y/d_1	C	$F \times d_1/V_1$	V/V_1
8.41	1.32	0.486	0.835	0.660
22.43	1.32	0.198	0.688	0.594
50.48	3.00	0.063	0.169	0.242

(B) $Fr_1 = 11.2$, $Re = 8.3 \times 10^4$, $d_1 = 0.01783$ m, $x_1 = 0.75$ m

Fig. 13. Bubble chord time distributions in the air–water shear layer at the characteristic location where $F = F_{max}$.

time in a 0.25 ms chord time interval. For example, the probability of bubble chord time from 1 to 1.25 ms is represented by the column labelled 1 ms. Bubble chord times larger than 10 ms are regrouped in the last column (>10 ms).

The experimental data showed systematically a number of features. First note the broad spectrum of bubble chord times at each location (Figs. 13 and 14). The range of bubble chord times extended over several orders of magnitude, including at low void fractions, from less than 0.1 ms to more than 20 ms. Second the distributions were skewed with a preponderance of small bubble chord time relative to the mean. In Fig. 13, corresponding to the air–water shear region, the probability of bubble chord time is the largest for chord times between 0.5 and 1 ms. In Fig. 14, the mode is about 0.5–2 ms and the result was typical of the upper free-surface region. The probability distribution functions of bubble chord time tended to follow in average a log-normal distribution, although a gamma distribution provided also a good fit. Note that a similar finding was observed by Chanson (2007).

Third, it is noted that the bubble chord time distributions had a similar shape at most vertical elevations y/d_1 although the air–water structures may differ substantially. This is seen by comparing Figs. 13 and 14. Although the quantitative values differed, the overall shape of the bubble chord time was similar.

In the free-surface region, the data showed a large amount of bubble chord times larger than 10 ms (Fig. 14). The results were consistent with the visual observations indicating some large air bubbles and a foamy bubbly flow structure next to the free-surface (Fig. 3). In Fig. 14B, the bubble chord time data are also compared with the chord time distribution in the upstream flow region at $(x - x_1)/d_1 = -11.2$. The comparison suggested some similarity,

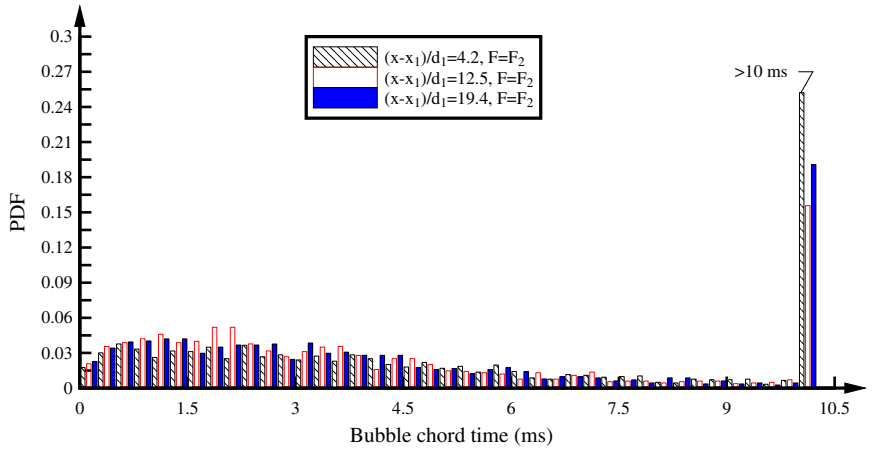

$(x-x_1)/d_1$	y/d_1	C	$F \times d_1/V_1$	V/V_1
4.17	3.11	0.519	0.248	--
12.50	3.58	0.422	0.247	--
19.44	6.42	0.380	0.146	--

(A) $Fr_1 = 7.5$, $Re = 5.6 \times 10^4$, $d_1 = 0.018$ m, $x_1 = 0.75$ m

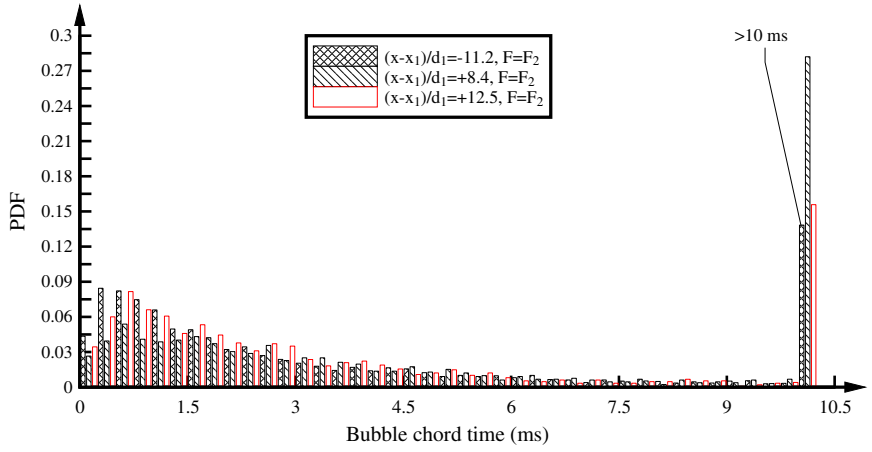

$(x-x_1)/d_1$	y/d_1	C	$F \times d_1/V_1$	V/V_1	Remark
-11.2	1.04	0.486	0.260	0.93	Upstream flow
8.41	4.68	0.721	0.112	--	Hydraulic jump roller
22.43	6.37	0.275	0.126	--	Hydraulic jump roller

(B) $Fr_1 = 11.2$, $Re = 8.3 \times 10^4$, $d_1 = 0.01783$ m, $x_1 = 0.75$ m - Comparison with the upstream flow properties

Fig. 14. Bubble chord time distributions in the upper free-surface region at the characteristic location where $F = F_2$.

although there were some basic differences: (a) the upstream flow was little aerated, and (b) the bubble chord times were smaller in the free-surface region of the upstream flow.

5.2. Bubble clustering

In the air–water flows, the void fraction and bubble count rate were some gross parameters that could not describe the air–water structures nor the interactions between entrained bubbles and turbulent shear. The present experimental results demonstrated a broad spectrum of bubble chord times extending over several orders of magnitude and the distributions of chord times were skewed with a preponderance of small bubbles relative to the mean (Figs. 13 and 14). Some signal processing provided further information on the longitudinal structure of the air–water flow including bubble clustering. The study of particle clustering events is relevant to infer whether the formation frequency responds to some particular frequencies of the flow.

When two bubbles are closer than a particular time/length scale, they can be considered a group of bubbles: i.e., a cluster. The characteristic water time/length scale may be related to the water chord statistics or to the near-wake of the preceding particle (Chanson and Toombes, 2002; Chanson and Carosi, 2007). Herein the latter approach was applied following Chanson et al. (2006). Two bubbles were considered parts of a cluster when the water chord time between the bubbles was less than the bubble chord time of the lead particle. That is, when a bubble trailed the previous bubble by a short time/length, and was in the near-wake of

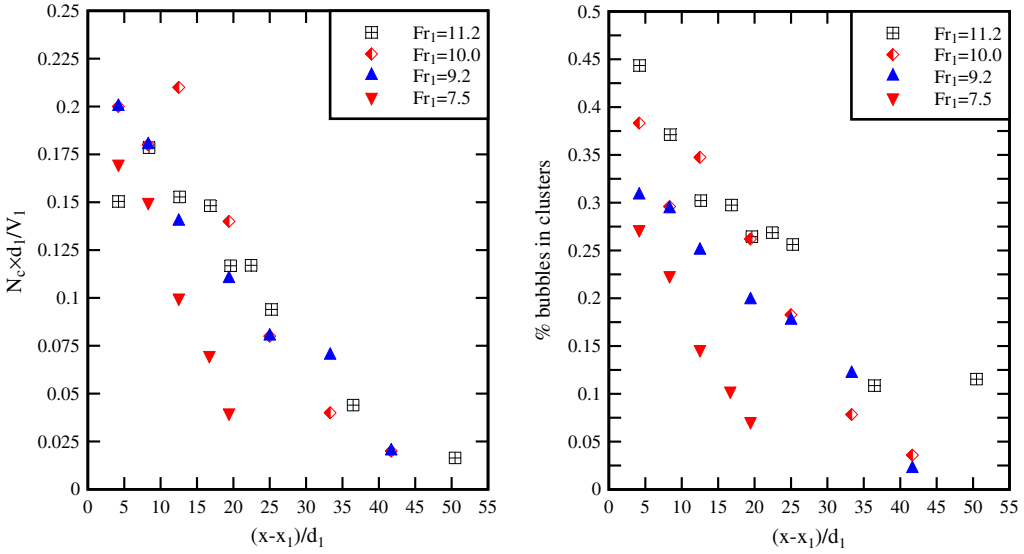

(A, Left) Dimensionless number of cluster per second $N_c \times d_1/V_1$

(B, Right) Percentage of bubbles in clusters

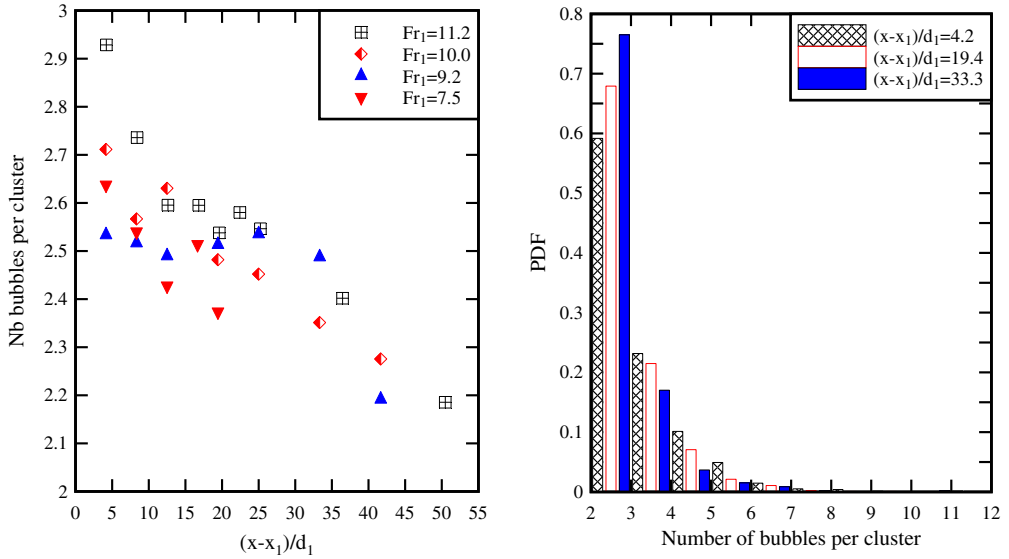

(C, Left) Number of bubbles per cluster

(D, Right) Probability distribution functions of the number of bubbles per cluster for $Fr_1 = 10.0$

Fig. 15. Characteristics of bubble clusters in the air–water shear layer at the locations where $F = F_{max}$ ($y = Y_{Fmax}$).

and could be influenced by the leading particle. Note the criterion does not rely upon the velocity measurement technique, but implies that the streamwise velocity is positive.

Fig. 15 presents some typical characteristics of the bubble clusters in the developing shear layer. All the data were recorded at the characteristic location $y = Y_{Fmax}$ where the bubble count rate was maximum ($F = F_{max}$). Fig. 15 includes the longitudinal distributions of number of clusters per second, the percentage of bubbles in clusters, the average number of bubbles per cluster, and the probability distribution function of the number of bubbles per cluster for $Fr_1 = 10$.

The experimental results showed systematically a number of trends. The number of clusters per second was substantial in the air–water shear layer, reaching up to 50 clusters per second for $Fr_1 = 10$ and 11. Further the number of clusters decreased rapidly with increasing longitudinal distance (Fig. 15A). The present data showed an exponential decay in the number of clusters:

$$\frac{N_c \times d_1}{V_1} \propto \exp\left(-\frac{x - x_1}{d_1}\right) \quad (14)$$

where N_c is the number of clusters per second.

The experimental results highlighted that a significant proportion of bubbles were parts of a cluster structure in the air–water shear zone. That is, more than one-third of all bubbles in the beginning of the shear layer ($(x - x_1)/d_1 < 10$) for $7.5 < Fr_1 < 11.2$. The percentage of bubbles in clusters decreased with increasing longitudinal distance as seen in Fig. 15B. The present findings differed from the results of Chanson (2007) who found only a small proportion of bubbles in clusters. While a different cluster criterion was used by Chanson (2007), it is believed that the key difference was the larger range of inflow Froude numbers tested in the present study. The present results showed indeed that the proportion of bubbles forming some clusters was the largest at the largest Froude numbers ($9.2 < Fr_1 < 11.2$) (Fig. 15B).

In average, the number of bubbles per cluster ranged from 2.7 down to 2.2 and decreased with increasing distance from the jump toe (Fig. 15C and D). The longitudinal pattern is illustrated in Fig. 14D showing the probability distribution function of the number of bubbles per clusters at three longitudinal locations for one experiment ($Fr_1 = 10$). It is however important to stress that the present study focused on the longitudinal flow structure and it did not account for bubble travelling side-by-side.

A comparative analysis was conducted on the bubble chord times, between all the bubbles and the bubbles in clusters only. A typical comparison is presented in Fig. 16. The results showed that the distribution of bubble chord times were comparable and

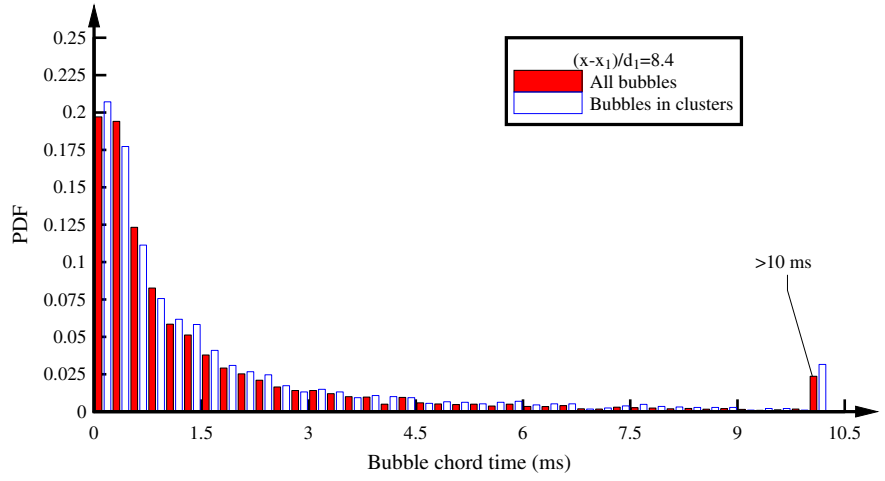

(A) $(x\text{-}x_1)/d_1 = 8.4$, $F = F_{max} = 219$ Hz, $N_c = 46.9$ Hz

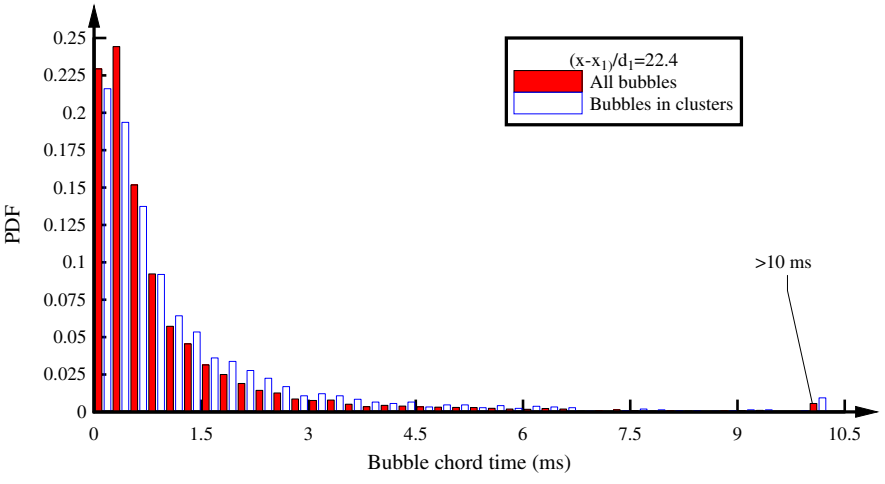

(B) $(x\text{-}x_1)/d_1 = 22.4$, $F = F_{max} = 181$ Hz, $N_c = 30.7$ Hz

Fig. 16. Probability distribution functions of bubble chord time in the air–water shear layer: comparison between all the bubbles and the bubbles forming parts of a cluster structure ($Fr_1 = 11.2$, $Re = 8.3 \times 10^4$, $d_1 = 0.0178$ m, $x_1 = 0.75$ m).

nearly identical for both the whole bubble sample and the bubbles in cluster structures. Simply there was no preferential bubble chord in the clusters as illustrated in Fig. 16.

The findings contradict the earlier study of Chanson (2007) based upon an inter-particle arrival time analysis. It is believed that a major issue was the assumptions underling the inter-particle arrival time analysis (Edwards and Marx, 1995; Heinlein and Fritsching, 2006). The method considers an ideal dispersed flow driven by a superposition of Poisson processes assuming non-interacting particles. The latter assumption (non-interacting particles) is incorrect in the developing shear layer of a hydraulic jump where the air bubbles are subjected to a wide range of interactions including bubble trapping in the large-scale vortices, bubble breakup by turbulent shear, and bubble collisions and coalescence.

6. Conclusion

The hydraulic jump is a singularity in terms of the flow depth, and the velocity and pressure fields, associated with the development of large-scale turbulence in the roller and some air bubble entrainment. An experimental study was performed herein in some hydraulic jumps with partially-developed inflow with large Froude numbers. Some detailed air–water flow measurements were conducted in a relatively large-size facility ($5.1 < Fr_1 < 11.2$ and $4.0 \times 10^4 < Re < 8.3 \times 10^4$).

In the developing shear layer, the distributions of void fractions may be modelled by a convective transport equation. The analytical solution of Chanson (1995) was refined and the experimental data demonstrated a close agreement with the theoretical developments. The turbulent air bubble mixing coefficient was observed to be independent of the Froude and Reynolds numbers. However it increased linearly with the distance from the jump toe in a manner somehow similar to the momentum exchange coefficient in a developing shear layer.

The experimental observations highlighted a significant air entrainment in the jump roller as well as some spray and splashing above the roller. The observations of jump toe fluctuations were close to earlier studies, and the new data showed that the jump toe oscillation frequency was equal to the production rate of large-scale vortical structures in the developing shear layer. Some video observations highlighted that the average advection speed of these large coherent structures was in average $V_{ej}/V_1 \approx 0.32$ in the developing shear layer. The basic air–water flow properties presented the same trends as earlier studies performed with lower Froude numbers. The void fraction distributions presented a local maximum in the air–water shear layer and its value decreased quasi-exponentially with increasing distance from the jump toe. The air–water mixing layer was characterised by a maximum in bubble count rate. The depth-averaged void fraction data demonstrated a large amount of entrained air as well as a rapid de-aeration of the jump roller. The velocity profiles followed closely some wall jet equations.

The bubble chord time distributions showed a broad range of entrained bubble chord times spreading over two orders of magnitudes. A detailed analysis of the longitudinal structure of the air and water chords suggested a significant proportion of bubble clustering in the developing shear region, especially close to the jump toe. In average the number of bubbles per clusters ranged from about 2.7 down to 2.2 with increasing distance from the jump toe. The data showed further that, in the shear layer, there was no preferential bubble chord time in the cluster structures. Overall the study highlighted some seminal features of the air–water shear layer in hydraulic jumps with large Froude numbers ($5.1 < Fr_1 < 11.2$). The transport of air in the mixing zone was a convective transport process, although there was some rapid flow de-aeration for all Froude numbers.

Acknowledgments

The author thanks Ben Hopkins and Hugh Cassidy who conducted carefully and thoroughly the experiments as part of their undergraduate thesis project. He acknowledges also the technical assistance of Graham Illidge and Clive Booth (The University of Queensland). The author thanks further Dr. Frédéric Murzyn (ESTACA Laval, France) for his helpful comments.

References

Avery, S.T., Novak, P., 1978. Oxygen transfer at hydraulic structures. J. Hydraulic Eng. Div., ASCE 104, 1521–1540.
Babb, A.F., Aus, H.C., 1981. Measurements of air in flowing water. J. Hydraulic Eng. Div., ASCE 107, 1615–1630.
Brown, G.L., Roshko, A., 1974. On the density effects and large structure in two-dimensional mixing layers. J. Fluid Mech. 64, 775–816.
Chanson, H., 1995. Air entrainment in two-dimensional turbulent shear flows with partially developed inflow conditions. Int. J. Multiphase Flow 21, 1107–1121.
Chanson, H., 1997. Air Bubble Entrainment in Free-Surface Turbulent Shear Flows. Academic Press, London, UK. 401 p. (ISBN 0-12-168110-6).
Chanson, H., 2002. Air–water flow measurements with intrusive phase-detection probes. Can we improve their interpretation? J. Hydraulic Eng., ASCE 128, 252–255.
Chanson, H., 2005. Physical modelling of the flow field in an undular tidal bore. J. Hydraulic Res., IAHR 43, 234–244.
Chanson, H., 2007. Bubbly flow structure in hydraulic jump. Eur. J. Mech. B/Fluids 26, 367–384. doi:10.1016/j.euromechflu.2006.08.001.
Chanson, H., 2009. Current knowledge in hydraulic jumps and related phenomena. A survey of experimental results. Eur. J. Mech. B/Fluids 28, 191–210. doi:10.1016/j.euromechflu.2008.06.004.
Chanson, H., 2009b. Advective diffusion of air bubbles in hydraulic jumps with large Froude numbers: an experimental study. Hydraulic Model Report No. CH75/09, School of Civil Engineering, The University of Queensland, Brisbane, Australia, 89 p. and three videos (ISBN 9781864999730).
Chanson, H., Brattberg, T., 2000. Experimental study of the air–water shear flow in a hydraulic jump. Int. J. Multiphase Flow 26, 583–607.
Chanson, H., Carosi, G., 2007. Advanced post-processing and correlation analyses in high-velocity air–water flows. Environ. Fluid Mech. 7, 495–508. doi:10.1007/s10652-007-9038-3.
Chanson, H., Toombes, L., 2002. Air–water flows down stepped chutes: turbulence and flow structure observations. Int. J. Multiphase Flow 27, 1737–1761.
Chanson, H., Aoki, S., Hoque, A., 2006. Bubble entrainment and dispersion in plunging jet flows: freshwater versus seawater. J. Coastal Res. 22, 664–677. doi:10.2112/03-0112.1. May.
Crank, J., 1956. The Mathematics of Diffusion. Oxford University Press, London, UK.
Crowe, C., Sommerfield, M., Tsuji, Y., 1998. Multiphase Flows with Droplets and Particles. CRC Press, Boca Raton, USA. 471 p.
Edwards, C.F., Marx, K.D., 1995. Multipoint statistical structure of the ideal spray, part I: fundamental concepts and the realization density. Atomization Sprays 5, 435–455.
Goertler, H., 1942. Berechnung von Aufgaben der freien Turbulenz auf Grund eines neuen Näherungsansatzes. Z.A.M.M. 22, 244–254 (in German).
Gualtieri, C., Chanson, H., 2007. Experimental analysis of Froude number effect on air entrainment in the hydraulic jump. Environ. Fluid Mech. 7, 217–238. doi:10.1007/s10654-006-9016-1.
Habib, E., Mossa, M., Petrillo, A., 1994. Scour downstream of hydraulic jump. In: Proceedings of the Conference on Modelling, Testing & Monitoring for Hydro Powerplants, International Journal on Hydropower & Dams, Budapest, Hungary, pp. 591–602.
Hager, W.H., 1992. Energy Dissipators and Hydraulic Jump. Kluwer Academic Publishers, Water Science and Technology Library, vol. 8, Dordrecht, The Netherlands, 288 p.
Heinlein, J., Fritsching, U., 2006. Droplet clustering in sprays. Exp. Fluids 40, 464–472.
Kucukali, S., Chanson, H., 2008. Turbulence measurements in hydraulic jumps with partially-developed inflow conditions. Exp. Therm. Fluid Sci. 33, 41–53. doi:10.1016/j.expthermflusci.2008.06.012.
Long, D., Rajaratnam, N., Steffler, P.M., Smy, P.R., 1991. Structure of flow in hydraulic jumps. J. Hydraulic Res., IAHR 29, 207–218.
Mossa, M., Tolve, U., 1998. Flow visualization in bubbly two-phase hydraulic jump. J. Fluids Eng., ASME 120, 160–165.
Murzyn, F., Chanson, H., 2008. Experimental assessment of scale effects affecting two-phase flow properties in hydraulic jumps. Exp. Fluids 45, 513–521. doi:10.1007/s00348-008-0494-4.
Murzyn, F., Chanson, H., 2009. Experimental investigation of bubbly flow and turbulence in hydraulic jumps. Environ. Fluid Mech. 9, 143–159. doi:10.1007/s10652-008-9077-4.

Murzyn, F., Mouaze, D., Chaplin, J.R., 2005. Optical fibre probe measurements of bubbly flow in hydraulic jumps. Int. J. Multiphase Flow 31, 141–154.
Rajaratnam, N., 1962. An experimental study of air entrainment characteristics of the hydraulic jump. J. Inst. Eng. India 42, 247–273.
Rajaratnam, N., 1965. The hydraulic jump as a wall jet. J. Hydraulic Div., ASCE 91, 107–132 (Discussion: vol. 92, pp. 110–123; vol. 93, pp. 74–76).
Rajaratnam, N., 1967. Hydraulic jumps. In: Chow, V.T. (Ed.), Advances in Hydroscience, vol. 4. Academic Press, New York, USA, pp. 197–280.
Rajaratnam, N., 1976. Turbulent jets. Development in Water Science, vol. 5. Elsevier Scientific, New York, USA.
Resch, F.J., Leutheusser, H.J., 1972. Le Ressaut Hydraulique: Mesure de Turbulence dans la Région Diphasique ('The Hydraulic Jump: Turbulence Measurements in the Two-Phase Flow Region'). Jl La Houille Blanche, pp. 279–293 (in French).
Schlichting, H., 1979. Boundary Layer Theory, seventh ed. McGraw-Hill, New York, USA.
Thandaveswara, B.S., 1974. Self aerated flow characteristics in developing zones and in hydraulic jumps. Ph.D. thesis, Department of Civil Engineering, Indian Institute of Science, Bangalore, India, 399 p.
Toombes, L., 2002. Experimental study of air–water flow properties on low-gradient stepped cascades. Ph.D. thesis, Department of Civil Engineering, The University of Queensland, Brisbane, Australia.
Valle, B.L., Pasternack, G.B., 2006. Air concentrations of submerged and unsubmerged hydraulic jumps in a bedrock step-pool channel. J. Geophys. Res. 111, 12. doi:10.1029/2004JF000140. paper F030l6.
Wisner, P., 1965. Sur le Rôle du Critère de Froude dans l'Etude de l'Entraînement de l'Air par les Courants à Grande Vitesse ('On the Role of the Froude Criterion for the Study of Air Entrainment in High Velocity Flows'). In: Proceedings of the 11th IAHR Congress, Leningrad, USSR, paper 1.15 (in French).